Gate-tuned differentiation of surface-conducting states in $Bi_{1.5}Sb_{0.5}Te_{1.7}Se_{1.3}$ topological-insulator thin crystals

Janghee Lee, Joonbum Park, Jae-Hyeong Lee, Jun Sung Kim, and Hu-Jong Lee*
Department of Physics, Pohang University of Science and Technology, Pohang 790-784, Republic of Korea
(Received 12 October 2012; published 26 December 2012)

Using field-angle, temperature, and back-gate-voltage dependence of the weak antilocalization (WAL) and universal conductance fluctuations of thin $Bi_{1.5}Sb_{0.5}Te_{1.7}Se_{1.3}$ topological-insulator single crystals, in combination with gate-tuned Hall resistivity measurements, we reliably separated the surface conduction of the topological nature from both the bulk conduction and topologically trivial surface conduction. We minimized the bulk conduction in the crystals and back-gate tuned the Fermi level to the topological bottom-surface band while keeping the top surface insensitive to back-gating with the optimal crystal thickness of ∼100 nm. We argue that the WAL effect occurring by the coherent diffusive motion of carriers in relatively low magnetic fields is more essential than other transport tools such as the Shubnikov–de Hass oscillations for confirming the conduction by the topologically protected surface state. Our approach provides a highly coherent picture of the surface transport properties of topological insulators and a reliable means of investigating the fundamental topological nature of surface conduction and possible quantum-device applications related to momentum-locked spin polarization in surface states.

DOI: 10.1103/PhysRevB.86.245321 PACS number(s): 73.20.At, 73.25.+i, 73.23.−b, 72.20.−i

I. INTRODUCTION

Similar to an ordinary-band insulator, a topological insulator (TI) has a bulk energy gap in its band structure, which is generated by a strong spin-orbit interaction. The topological phase transition, brought about by the band inversion in the material, induces Dirac-fermionic surface-conducting channels.[1–5] This topologically protected surface state (TSS) has a helical spin texture that is robust to small perturbations conserving the time-reversal symmetry, and thus prohibiting backscattering by nonmagnetic impurities.[6–8]

Diverse transport studies were conducted to characterize the TSS. In general, however, as-grown TIs are n- or p-doped so that the surface conduction can be predominated by bulk conduction.[9–11] Efforts have been made to reduce the bulk conduction by tuning the Fermi level (E_F) into the bulk band gap.[10–22] Even with these efforts, however, critical inconsistencies were present in the previous transport measurements. For instance, in bulk TIs with a thickness larger than ∼μm, two-dimensional (2D) Shubnikov–de Haas oscillations (SdHOs) were observed. Nonetheless, the weak antilocalization (WAL) effect, relevant to the TSS, was often absent in the corresponding measurements, or, if present, did not fit well to the 2D Hikami-Larkin-Nagaoka (HLN) WAL expression[15,23–32] (see Appendix A). In a TI, the WAL effect is generated by a strong spin-orbit interaction and the consequent destructive interference between two electron waves traveling along a diffusive closed path in a time-reversal manner.[32–34]

These inconsistencies between the 2D SdHO and WAL were also observed in thinner flakes, with a thickness less than ∼μm.[21,22,35,36] Furthermore, previous 2D-SdHO observations[15,22,25–28,35,36] may not have been fully relevant to the surface conduction by the TSS.[27,37,38] Accurately identifying the Berry-phase shift associated with the TSS requires measurements in very strong magnetic fields, with careful Landau-level indexing.[38] In most of the previous studies, however, the 1/2 Berry-phase shift was determined based on observations in relatively weak magnetic fields.[15,22,26,28,35,36] Ambipolar characters with back gating were also observed in the transport of TIs, which were assumed to be associated with the TSS. Here, however, the WAL effect was absent in the samples with relatively high carrier densities.[19–21] The WAL effect observed in some of these ambipolar-transport samples were reported to arise from the coupling between the surface and the bulk bands, rather than the TSS exclusively.[16–18,39–44]

It is an extremely difficult task to reliably separate the TSS from other conductance contributions. In this study, we minimized the bulk conduction using high-quality $Bi_{1.5}Sb_{0.5}Te_{1.7}Se_{1.3}$ (BSTS) TI single crystals, with E_F lying in the bulk gap without gating. We confirmed that the WAL effect and universal conductance fluctuations (UCFs) indeed arose from the top and bottom surfaces. By back-gate tuning the WAL characteristics, we identified the TSS conducting characteristics and the coupling between the TSS and the topologically trivial two-dimensional electron gas (2DEG) states that emerged due to band bending near the bottom surface. The ambipolar Hall resistivity of the bottom surface was consistent with the back-gate-voltage (V_{bg}) dependence of the longitudinal resistance of the TSS. This study provides a reliable means of differentiating the TSS of TIs from those of the bulk conducting state and the topologically trivial 2DEG states, along with a highly coherent picture of the topological surface transport properties of TIs.

II. SAMPLE PREPARATION AND MEASUREMENTS

BSTS single crystals were grown using the self-flux method.[12,13] Stoichiometric mixture of high-purity starting materials [Bi(5N), Sb(5N), Te(5N), Se(5N)] were loaded in an evacuated quartz ampoule, which was then heated up to 850 °C. After annealing at 850 °C for two days to enhance the material homogeneity, the melt mixture was slowly cooled down to 600 °C for a week. Before complete furnace cooling it was kept at 600 °C for one more week to further improve the crystallinity. The stoichiometry and the high crystallinity

of the single crystals were confirmed by the energy dispersive spectroscopy and the x-ray diffraction, respectively.

The bulk transport properties were examined using ~100 μm-thick cleaved bulk crystals. For detailed characterization of transport properties with back gating, BSTS flakes, which are 22 to 230 nm in their thickness, were mechanically exfoliated onto a Si substrate capped with a 300-nm-thick oxidized layer. This was then followed by standard electron (e)-beam patterning and e-gun evaporation of Ti/Au (10 nm/100−350 nm thick) bilayer electrodes and contact leads. For thick crystals, the electrode contacts were prepared using silver paste. In total, four thick bulk crystals and six thin flakes were investigated using standard lock-in measurements, varying T from 290 to 4.2 K.

III. RESULTS AND DISCUSSION

A. Thickness and temperature dependence of resistance

The T dependence of the resistivity ρ_{xx} of the thick bulk crystals of BSTS in Fig. 1(a) exhibits conventional semiconducting behavior down to ~40 K. A fit of $\rho_{xx}(T)$ to the Arrhenius law renders the activation energy of $E_a = 26.1$, 21.3, 31.6, and 20.7 meV for samples B1, B2, B3, and B4 [inset in Fig. 1(a) corresponds to sample B3], consistent with previous studies.[14] However, the resistance is saturated for T below ~40 K, which indicates the emergence of additional conducting channels. This behavior was more pronounced in the thin flakes. Figure 1(b) shows a clear semiconductor-metal transition as the thickness of the flakes decreases. The variation of $\rho_{xx}(T)$ with the flake thickness can be interpreted in terms of surface-conducting channels in the presence of a bulk insulating gap, as illustrated in Fig. 1(f). With E_F inside the bulk energy gap, the residual bulk conduction by carriers thermally activated from an impurity band was dominant in the thick crystals [Fig. 1(a)]. Thin flakes, however, with less bulk conductance, exhibited metallic behavior. One can confirm this behavior by modeling the simple form for total sheet conductance as follows:

$$G_\square = G_s + \sigma_b t, \tag{1}$$

where G_s is the surface sheet conductance, σ_b is the bulk conductivity, and t is the thickness of crystals. Here, G_s includes the conduction through the 2DEG layer [see Fig. 1(f)] in the potential well formed by surface band bending, as well as the conduction by the TSS.[45–47] Fitting the observed results to Eq. (1) [Fig. 1(c)], σ_b is estimated to be 86.9 and 26.7 (e^2/h) μm^{-1} at 290 and 4.2 K, respectively. These values are at least two orders of magnitude smaller than the ones reported previously for Bi_2Se_3,[19] indicating that our BSTS single crystals were highly "bulk insulating". Assuming the range of surface band bending at the surface to be ~30 nm (see Appendix B) in sample F4, the relative weight of the bulk to the surface conductance becomes $\sigma_b t/G_s \sim 26\%$ (6%) at 290 K (4.2 K).

B. Angle and temperature dependence of WAL and UCF

The surface-dominant conduction at low T becomes more evident in the field-angle dependence of the magnetoresistance (MR). Figure 2(b) shows that all of the MR curves taken

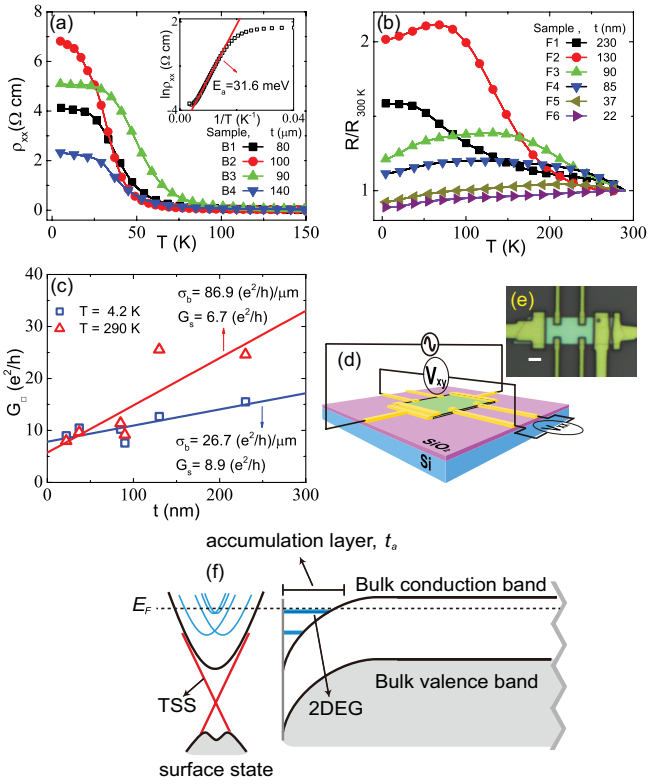

FIG. 1. (Color online) (a) T dependence of the bulk crystal resistivity of the TI. Inset: Arrhenius-law fitting for the sample B3. (b) T dependence of the normalized resistance of thin flakes. (c) Thickness dependence of the sheet conductance of thin flakes at 290 K (triangles, red online) and 4.2 K (squares, blue online). Solid lines are best fits to Eq. (1). (d) Schematic measurement configuration and (e) the optical image of the sample F4 with invasive lead contacts. The scale bar is 2 μm. (f) Schematic band structure near a surface of our TI samples. The crossed lines (red online) represent the TSS. t_a represents the range of surface band bending (or the range of carrier accumulation) on the surface. Horizontal thick lines at t_a (blue online) represent the 2DEG formed at the surface due to the surface band bending. Double-parabolic curves (blue online) are Rashba-split bands of the 2DEG. Horizontal dashed line corresponds to the Fermi level.

at different field angles [Fig. 2(a)], plotted as a function of the normal component of the field ($B_\perp$), merge into a single universal curve (see Appendix C for the discussion on the MR feature in in-plane fields; $\theta = 90°$). Even the positions of the UCF peaks agree with each other when plotted as a function of $B_\perp$ [Fig. 2(c)]. These features strongly indicate that the MR in our sample was almost completely dominated by surface conduction over the entire field range of our measurements. Previously, the $\cos(\theta)$ angle dependence of the MR was observed only in the low-field range of B within a fraction of tesla.[44,48]

The 2D nature was identified more quantitatively from the T dependence of the MR. Figure 2(d) is the T dependence of WAL effects and the best fits of $\Delta G_{xx}(B)$ to Eq. (2), from which we obtained the T dependence of the phase relaxation length l_ϕ as shown in Fig. 2(f) (more details of the WAL effect are discussed below). Figure 2(e) shows the T dependence of δG, with the corresponding T dependence of

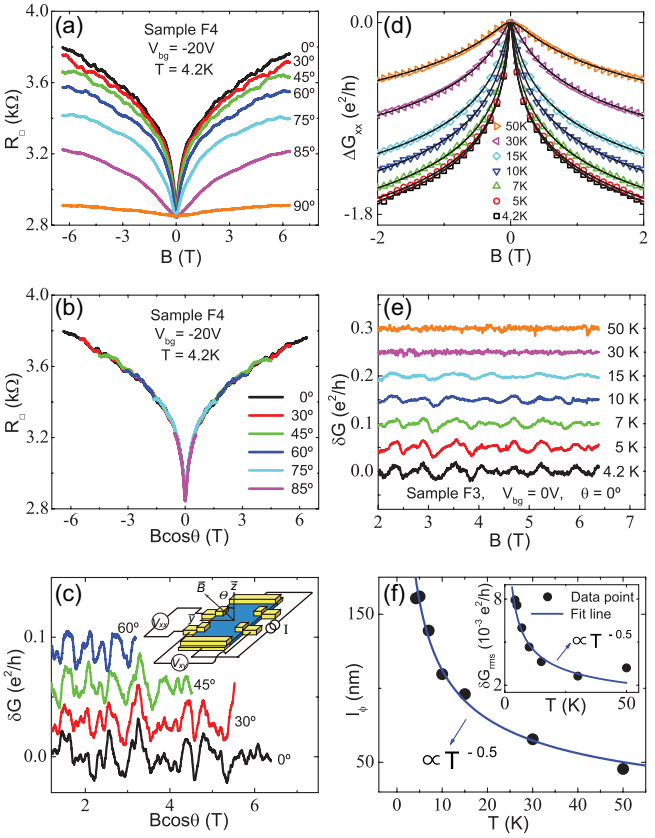

FIG. 2. (Color online) (a) Sheet resistance $R_\square$ vs B and (b) $R_\square$ vs $B\cos\theta$ for different field angles at $V_{bg} = -20$ V for sample F4. (c) $\delta G = G(B) - G_0(B)$ vs $B\cos\theta$ extracted from the data in (b), where $G_0(B)$ is the background of $G(B)$ $[=1/R_\square(B)]$. For clarity, each curve is shifted vertically by 0.03 e^2/h. Inset: Schematic measurement configuration. (d) $\Delta G_{xx}(B) = G_{xx}(B) - G_{xx}(B=0)$ vs B at different T for sample F3. Solid lines are best fits to Eq. (2). (e) T dependence of δG of sample F3 extracted from the data in (d). For clarity, each curve is shifted vertically by 0.05 e^2/h. (f) T dependence of the phase-relaxation length l_ϕ obtained from (d). Inset: T dependence of the root-mean-square of δG extracted from the data in (e).

the UCF amplitude $\delta G_{\rm rms}$ shown in the inset of Fig. 2(f). In a 2D system with a sample dimension of $L \gg l_\phi$, l_ϕ scales as $T^{-0.5}$ for inelastic scattering by electron-electron interaction, and $\delta G_{\rm rms}$ is proportional to l_ϕ.[49–52] In Fig. 2(f), both l_ϕ and $\delta G_{\rm rms}$ scale as $T^{-0.5}$, in good agreement with the theoretical predictions, indicating that the dominant inelastic scattering in the surface-conducting channels of our BSTS flakes was due to the electron-electron interaction.

C. Back-gate dependence of WAL

Up to this point, results from our BSTS consistently indicate that the bulk conduction was negligible, and that both WAL and UCF had a 2D nature. The WAL in the TSS arose from the Berry phase π caused by the helical spin texture. Since the Rashba-split 2DEG has the momentum-locked spin helicity [see Figs. 3(d), (e), and (f)], the topologically trivial 2DEG states also exhibit the WAL effect. Applying $V_{\rm bg}$, we confirmed that the WAL effect arose from surface conduction, in both TSS and the topologically trivial 2DEG, with negligible bulk conduction. According to the HLN theory, for a 2D system in the symplectic limit [i.e., in the limit of strong spin-orbit coupling ($\tau_\phi \gg \tau_{\rm so}, \tau_e$; τ_ϕ is the dephasing time, $\tau_{\rm so}$ the spin-orbit scattering time, and τ_e the elastic scattering time)] with a negligible Zeeman term, the magnetoconductance correction is given as follows:

$$\Delta G_{xx} = \alpha \frac{e^2}{2\pi^2\hbar}\left[\ln\left(\frac{\hbar}{4el_\phi^2 B}\right) - \psi\left(\frac{1}{2} + \frac{\hbar}{4el_\phi^2 B}\right)\right], \quad (2)$$

where ψ is the digamma function, e is the electronic charge, $\hbar$ is Planck's constant divided by 2π, and l_ϕ is the phase-relaxation length.[32] Because the WAL effect constitutes a prominent transport property of the TSS, the relationship between the parameter α and the number of conducting channels in the symplectic limit is essential to differentiating the transport nature of TIs.[53] Each 2D conducting channel in the symplectic limit contributes 0.5 to the value of α. If there are two independent 2D conducting channels in the symplectic limit, $\alpha = \alpha_1 + \alpha_2$ (α_i, corresponding to the channel i) and l_ϕ is replaced by the effective phase relaxation length (see Appendix D for details of the WAL fitting).

We confirmed that the back gating affected only the bottom-surface conductance for the 85∼90 nm-thick samples (F3 and F4) (see Appendix E). Figure 3(a) shows ΔG_{xx} vs B in color codes (online) as a function $V_{\rm bg}$. Here, the WAL effect occurs over the entire range of $V_{\rm bg}$ of this study with a maximum ΔG_{xx} at $V_{\rm bg} \sim -19$ V, the Dirac point of the TSS at the bottom surface [corresponding to the center diagram in Region II of Fig. 3(c)]. Figure 3(b) shows ΔG_{xx} curves for different values of $V_{\rm bg}$, which agree well with Eq. (2) (solid curves) over the entire range of B; the corresponding values of α are plotted in Fig. 3(g). For all $V_{\rm bg}$, α exceeds unity, indicating that more than two 2D conducting channels with the symplectic-limit behavior were involved in the surface conduction.

In Region II of Fig. 3(g), the TSS in the bottom surface contributes a value of 0.5 to α. This leaves $\alpha \sim 1$ for the top surface, which does not appear to be affected by $V_{\rm bg}$. Thus, we infer that the band bending near the top surface is like what is shown in Fig. 3(c). In the top surface, in addition to the TSS, the two Rashba-split channels in the trivial 2DEG layer also exhibit WAL in the symplectic limit.[45–47] However, the magnitude of α is reduced from 1.5 ($=0.5 \times 3$) to ∼1 due to interband scattering, where the degree of reduction depends on the scattering strength.[53] In Region I, E_F also enters the bulk conduction band (BCB) of the bottom surface. But, if the surface band bending is not enough to make a sufficient Rashba splitting in the 2DEG states as in Fig. 3(f), the band structure of the 2DEG would be similar to the unitary case,[32] where the scattering between the TSS and the topologically trivial 2DEG states is enhanced along with weakening of the WAL effect.[54] This reduces the value of α of the bottom surface down to ∼0.2−0.3, while leaving α unchanged at ∼1 for the top surface. If E_F is shifted deeper into the conduction band as to form a 2DEG on the bottom surface with a large-Rashba-split bulk subband [Fig. 3(d)], the WAL effect will be enhanced again, with the value of α larger than 0.5 as shown in Fig. 3(c) for the top surface.[53] In Region III, a similar reduction of α is

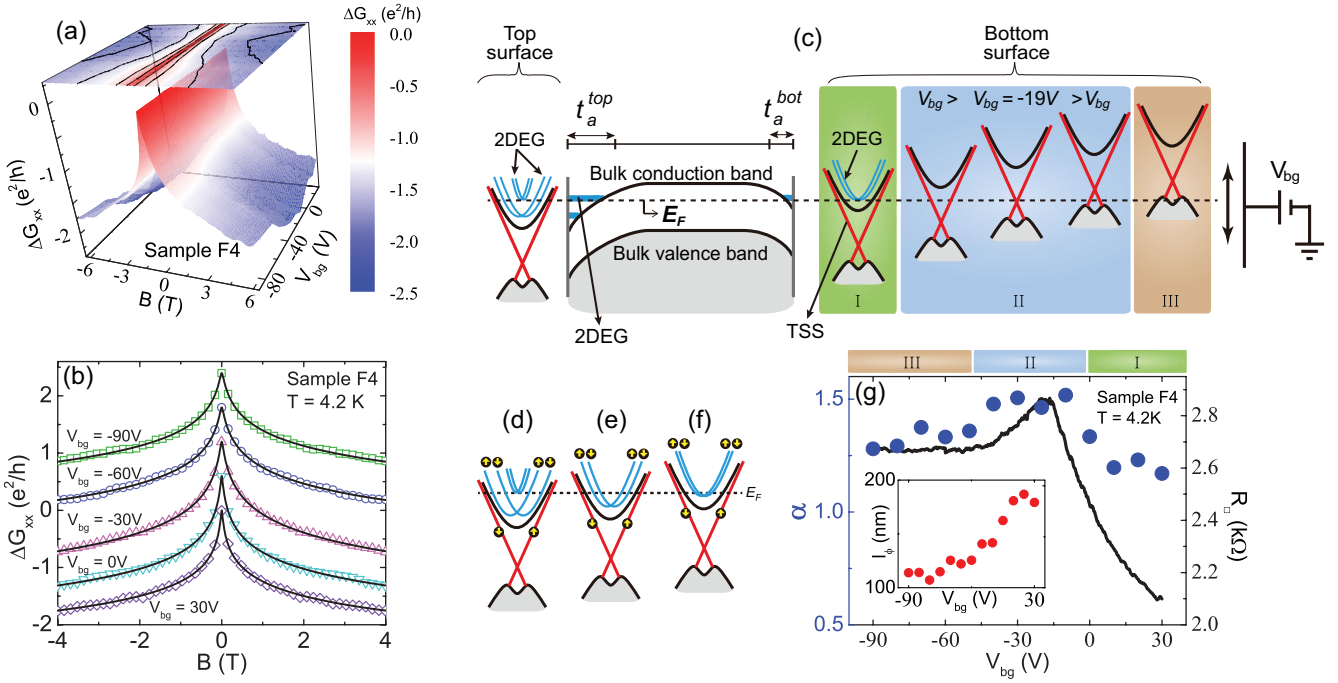

FIG. 3. (Color online) (a) ΔG_{xx} vs B in color codes (online) as a function $V_{\rm bg}$. (b) $\Delta G_{xx}(B)$ curves for different values of $V_{\rm bg}$. Solid lines are best fits to Eq. (2). For clarity, each curve is shifted vertically by $0.6e^2/h$. (c) Schematic band diagram relevant to the thin flakes used in this study. The crossed lines (red online) represent the TSS. $t_a^{\rm top}$ ($t_a^{\rm bot}$) represents the range of the carrier accumulation on the top (bottom) surface. Horizontal thick lines at $t_a^{\rm top}$ and $t_a^{\rm bot}$ (blue online) represent the 2DEG formed at the top and bottom surface due to the surface band bending. Double-parabolic curves (blue online) are Rashba-split bands of the 2DEG. Horizontal dashed line depicts the Fermi level. Regions I, II, and III represent the band structure for the corresponding regions denoted in (g). (d, e, f) Schematic diagram of the Rashba-split strength of 2DEG for different band bending. Up and down arrows indicate the spin texture. (g) $V_{\rm bg}$ dependence of α, obtained from best fits to Eq. (2). Solid curves are the $V_{\rm bg}$ dependence of $R_\square$. Inset: $V_{\rm bg}$ dependence of l_ϕ, also obtained from best fits to Eq. (2).

expected for the bottom surface, due to the enhanced scattering between the TSS and the bulk valence band (BVB). Thus, the variation of α with $V_{\rm bg}$ in Fig. 3(g) is the result of variation of the WAL in the bottom surface state.

The WAL effects reported previously on TIs with $\alpha \sim 0.5$[16,18,39–41] or $\alpha \sim 1$[17,21,42–44,55] contained a finite bulk contribution. $\alpha \sim 0.5$ corresponded to an effective single layer formed by the bulk and the two (top and bottom) surfaces, which are strongly coupled together. Meanwhile, $\alpha \sim 1$ corresponded to an effective single layer formed by the n-type bulk strongly coupled to the top surface, in association with the p-type bottom surface that was decoupled from the bulk by the formation of the depletion layer for a large negative value of $V_{\rm bg}$.[53] To the best of our knowledge, no previous reports have shown good fits to the symplectic-limit expression of Eq. (2) for fields up to several tesla, with α exceeding unity.[16–18,21,39–44,55] Although the good fits of our results to Eq. (2) without the Zeeman correction may be related to the recent report of small Landé g factor in TIs,[38,56,57] more studies are required to draw a definite conclusion on the issue.

D. Back-gate dependence of Hall resistivity

From the thickness, field angle, and temperature dependence of the resistance, we conclude that in our BSTS samples the electronic transport was dominated by the top and bottom surfaces. In this case, the Hall resistivity can be described by a standard two-band model as[58]

$$R_{xy} = -\left(\frac{B}{e}\right)\frac{(n_1\mu_1^2 + n_2\mu_2^2) + B^2\mu_1^2\mu_2^2(n_1+n_2)}{(|n_1|\,\mu_1 + |n_2|\,\mu_2)^2 + B^2\mu_1^2\mu_2^2(n_1+n_2)^2}. \tag{3}$$

Here, n_i and μ_i are the density and mobility of the carriers, respectively, in the ith conducting channel. The top ($i = 1$) and bottom ($i = 2$) surfaces constitute parallel conducting channels, with n_i being positive (negative) for n-type (p-type) carriers.[58] In sufficiently strong fields, R_{xy} converges to $R_{xy} = R_H^{\rm strong} B \approx -\frac{B}{e(n_1+n_2)}$. In weak fields ($B \approx 0$ T), Eq. (3) is reduced to

$$R_H^{\rm weak} = R_H^{\rm strong}\left[1 + \frac{n_1 n_2(\mu_1 \mp \mu_2)^2}{(n_1\mu_1 \pm n_2\mu_2)^2}\right]. \tag{4}$$

Here, the double signs are of the same order. The upper (lower) sign corresponds to $n_1, n_2 > 0$ ($n_2 < 0 < n_1$).

Figure 4(a) shows the results of analysis of the $V_{\rm bg}$ dependence of Hall resistivity from sample F4. For $V_{\rm bg} \geqslant 10$ V, the difference between the square (red online) and the circle (blue online), which means nonlinearity of R_{xy}, is very small, thus the R_{xy} curves are almost linear in B. As the $V_{\rm bg}$ is lowered to a negative value, the R_{xy} curves starts to bend and the nonlinearity of the R_{xy} increases as the $V_{\rm bg}$ decreases [curve in right inset in Fig. 4(a)]. In this region (e.g., $V_{\rm bg} = -10$ V), the slope of the tangent to R_{xy} at $B = 0$ T is larger than that

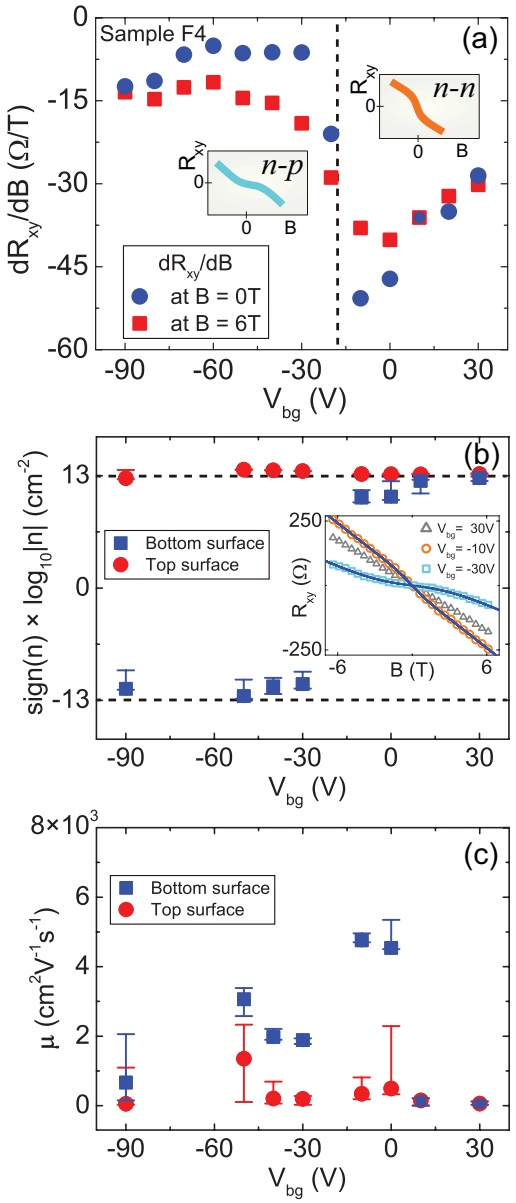

FIG. 4. (Color online) (a) V_{bg} dependence of the slope of the tangent to $R_{xy}(B)$ curves for Sample F4 at zero magnetic field (circles, blue online) and 6 T (squares, red online), respectively. The curves in right inset (orange online) and left inset (cyan online) represent the characteristic schematic feature of nonlinear R_{xy} curve when the sample is in the n-n state for $V_{bg} > -19$ V and in the n-p state for $V_{bg} < -19$ V. The vertical dashed line represents the boundary between the n-n and n-p states. (b), (c) V_{bg} dependencies of the carrier density and the mobility in the bottom and top surfaces of sample F4, which are obtained by fitting the R_{xy} data to Eq. (3). The dashed lines in (b) correspond to $|n| = 10^{13}\text{cm}^{-2}$. The inset in (b) shows the representative Hall resistivity curves for $V_{bg} = 30$ (linear dependence), -10 (n-n state, circle), and -30 V (n-p state, square). The solid lines are the best fits to Eq. (3).

at $B = 6$ T. However, the feature is reversed for $V_{bg} = -30$ V [curve in left inset in Fig. 4(a)] and the nonlinearity of R_{xy} decreases as the V_{bg} decreases. Using Eq. (4), it turned out that the change in the shape of the R_{xy} curve [from right inset to left inset in Fig. 4(a)] indicates the ambipolar transport of Dirac fermions between the n-n state (top: n-doped, bottom: n-doped) and the n-p state on TI surfaces.

If $\mu_1 \approx \mu_2$ and $n_1, n_2 > 0$ in Eq. (4), then $R_H^{\text{weak}} \approx R_H^{\text{strong}}$, corresponding to the region of $V_{bg} \gtrsim 15$ V in Fig. 4(a). Since the R_{xy} curves are almost linear in B, the carrier mobility is estimated to be $\mu_1, \mu_2 \sim 140\ \text{cm}^2/(\text{Vs})$ using the relationship $\mu = \frac{\sigma}{ne}$, which agrees with previous reports.[13,28,38] In this region [Region I in Fig. 3(c)] with E_F in the BCB, the mobility decreased due to the enhanced interband scattering.[45] As V_{bg} decreased, with E_F shifted to the TSS in Region II in Fig. 3(c), the mobility of the bottom surface was enhanced so that $\mu_1 \neq \mu_2$. In this case, if $n_1, n_2 > 0$, Eq. (4) leads to $|R_H^{\text{weak}}| > |R_H^{\text{strong}}|$, which corresponds to the curve for $V_{bg} = -10$ V in the inset of Fig. 4(b) [right inset in Fig. 4(a)]. Decreasing V_{bg} further, E_F shifted to a p-type region at the bottom surface. With $n_2 < 0$ and $|n_1| \gg |n_2|$, Eq. (4) leads to $|R_H^{\text{weak}}| < |R_H^{\text{strong}}|$, corresponding to the curve for $V_{bg} = -30$ V in the inset of Fig. 4(b) [left inset in Fig. 4(a)]. The change in the relative magnitude of the slopes of the tangent to $R_{xy}(B)$ (i.e., $|R_H^{\text{strong}}|$ and $|R_H^{\text{weak}}|$) for V_{bg} crossing -19 V clearly indicates ambipolar transport of the Dirac fermions between the n-n and n-p states on the TI surface. For $V_{bg} \lesssim -50$ V [Region III in Fig. 3(c)], with E_F in the BVB, scattering between the TSS and the BVB was enhanced once again.[59] The resulting suppression of μ_2, combined with an increase of n_2 in the range of $V_{bg} \lesssim -50$ V along with the relationship $\sigma_2 = n_2 e \mu_2$ for the bottom surface, may explain the low sensitivity of $R_\square$ to V_{bg} in Fig. 3(g).

Fitting the R_{xy} data to Eq. (3) gives more quantitative support for the analysis above on the V_{bg} dependence of the Hall resistivity. The inset of Fig. 4(b) shows the representative Hall resistivity for $V_{bg} = 30$, -10, and -30 V, where the solid curves are the best fits to Eq. (3) with the parameter values summarized in Figs. 4(b) and 4(c). n_1 in Fig. 4(b) is almost constant for all values of V_{bg}, while n_2 changes its sign between n and p types at $V_{bg} \sim -19$ V. This indicates ambipolar transport for the bottom surface with varying V_{bg} across the Dirac point, while the top surface remained mostly unaffected by back gating, consistent with earlier qualitative analysis of V_{bg} dependent Hall resistivity. This back-gating effect on the two surfaces was also confirmed by the mobility change. In Fig. 4(c), the best-fit values of μ_1 are almost insensitive to the variation of V_{bg}. However, μ_2 turns out to be significantly larger than μ_1 in the region, $-50\ \text{V} \leqslant V_{bg} \leqslant 0$ V, where E_F is assumed to be in the Dirac band of the bottom surface. The μ_2 enhancement possibly stems from the mobility increase as E_F shifts into the Dirac band of the bottom surface from the trivial 2DEG band (either conduction or valence), where μ_2 is reduced by the scattering between the TSS and the trivial 2DEG band. It should be noted that, with the invasive configuration of electrodes adopted in this study, the observed Hall voltage is bound to be underestimated. However, the qualitative V_{bg} dependence of the parameters in Eq. (3) remains valid.

IV. CONCLUSION

The 1/2 Berry-phase shift in SdHO is often adopted to examine the topological nature of surface transport. However,

very strong magnetic fields of $B \gtrsim 50$ T with careful Landau-level indexing, required for accurate determination of the Berry phase, have made it difficult to clearly differentiate the conductance by the TSS from that by the trivial 2D-conducting states. Observation of SdHO also requires relatively high mobility with a sufficiently long mean-free path to support the cyclotron orbital motion. In contrast, the observation of WAL, an intrinsic 2D effect, directly points to conduction by the TSS. Furthermore, WAL, which arises from the coherent diffusive motion of carriers, is not limited to the high mobility state. In this sense, the WAL effect, which was used primarily in this study, can be considered to be a more essential criterion than the SdHO for confirming the conduction by the TSS.

For flakes significantly thicker than an optimum thickness of ~80−90 nm, the bulk conductance cannot be neglected. On the other hand, as the range of band bending near the top and bottom surfaces begins to overlap for thinner flakes, independent gate control of the surface conduction would no longer be possible. Thus, our approach of separating the TSS by examining the transport characteristics specific to the 2D-topological nature in the optimal-thickness crystal flakes (in combination with back gating) provides a convenient means of investigating the fundamental topological nature of the surface conduction and the quantum-device applications associated with momentum-locked spin polarization in the surface state of TIs.

ACKNOWLEDGMENTS

H.J.L. thanks V. Sacksteder for valuable discussion. This work was supported by the National Research Foundation (NRF), through the SRC Center for Topological Matter [Grants No. 2011-0030788 (for H.J.L.) and No. 2011-0030785 (for J.S.K.)], the GFR Center for Advanced Soft Electronics (Grant No. 2011-0031640 for H.J.L.), and the Mid-Career Researcher Program (Grant No. 2012-013838 for J.S.K.).

APPENDIX A: POSSIBLE FORMATION OF MULTIPLE PARALLEL 2D CONDUCTING CHANNELS IN TIs

The weak antilocalization (WAL) in bulk topological insulator (TI) single crystals and thin TI flakes with high carrier density was reported previously.[22,25,31] However, the magnitude of the consequent conductance correction (ΔG) was larger than our results by one or two orders of magnitude. Since the magnitude of ΔG is proportional to the parameter α in Eq. (2) in the main text, which corresponds to the number of parallel conducting channels, one may suspect that multiple two-dimensional (2D) conducting channels connected in parallel were present for the conduction of TI in previous studies. A recent report[37] supports the inference. In Ref. 37, it was concluded that the observed quantized Hall effect and SdHO were not caused by the topologically protected surface state (TSS) but by many topologically trivial 2D conducting channels connected in parallel.

From the SdHO measurements, one can obtain the information on the dimensionality and carrier density of the conducting channels. In the SdHO analysis, the degeneracy "2" corresponds to the bulk band or the topologically trivial two-dimensional electron gas (2DEG) on the surface accumulation layer, while the degeneracy "1" corresponds to the TSS. In some previous studies,[27,60] the carrier density was estimated from the SdHO data adopting the degeneracy "1" under the assumption that the observed SdHO arose from the TSS. The carrier density estimated in this way was claimed to be relevant to the TSS, based on the fact that, with E_F lying in the TSS, the maximum carrier density is expected to be $0.5 \sim 0.8 \times 10^{13}$ cm^{-2} depending on the TI materials used. However, if the SdHO had arisen from the topologically trivial 2D conducting channels, the degeneracy should have been "2" with a doubled carrier density. In this case, however, a Dirac cone cannot accommodate all the carrier states estimated with the degeneracy "2" in Refs. 27 and 60 without the bulk conduction band or 2DEG states.

In fact, the SdHO frequencies themselves obtained in Ref. 37 and Refs. 27, 60 were not much different from each other. Thus, the difference in the carrier densities between Ref. 37 and Refs. 27, 60 resulted from the different degeneracy values adopted in the analysis. Depending on the degeneracy value used in the SdHO analysis, one may reach very different conclusions on the topological nature of the conducting channels involved in the SdHO data. In this sense, observation of the SdHO itself cannot confirm the existence of the TSS. Correctly identifying the Berry phase in strong magnetic fields is essential to confirming the TSS in TIs.[38]

APPENDIX B: SURFACE BAND BENDING

The surface band bending effect is a common feature of semiconductors. In particular, for narrow-gap semiconductors, the transport and electronic contact properties are strongly affected by the surface band bending. The materials which are identified as TIs are, in general, narrow-gap semiconductors whose band gap is about $100 \sim 300$ meV.[3] Since the energy levels of the surface state can be shifted up to a few hundred meV,[46,47,61] the surface band bending has a large influence on transport properties of TIs. But it has not been studied in depth to date.

The depth of the surface accumulation layer [t_a in Fig. 1(f) in main text] depends on the distribution of the local carrier density along the z axis.[62,63] For samples with the relatively high carrier density (i.e., if E_F lies in the bulk conduction band) t_a was calculated to be ~10−25 nm.[20,22,35,45–47] t_a can increase further as the carrier density decreases.[62,63] Since, in our sample, E_F lies in the bulk band gap with a low bulk carrier density, t_a can be longer than 25 nm.

In addition, in comparison with the bottom surface, the top surface is more exposed to chemicals and e-beam irradiation through the sample preparation processes. From the careful analysis provided in the main text, we concluded that these processes caused the band bending at the top surface, which was larger than that at the bottom surface, as illustrated in Fig. 3(c) in the main text.

APPENDIX C: IN-PLANE FIELD DEPENDENCE OF MAGNETORESISTANCE

Figure 5 shows the MR at $\theta = 90°$; direction of magnetic field is in parallel with the top and bottom surfaces of the

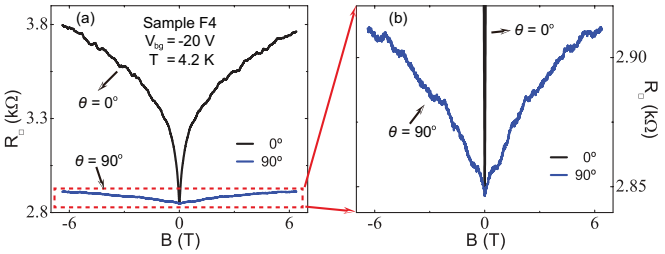

FIG. 5. (Color online) (a) The MR at $V_{bg} = -20$ V for different angles $\theta = 0°$ (black online) and $\theta = 90°$ (blue online) of sample F4. (b) An expanded view of the MR at $\theta = 90°$.

sample and perpendicular to the current direction [see Fig. 2(a) in main text]. If the conduction in our thin flakes was only through the two surfaces (top and bottom) and only the localization effect affected the MR, the MR should have vanished at $\theta = 90°$. As shown in Fig. 5, however, a small but finite MR exists at $\theta = 90°$.

The simplest inference is that the MR at $\theta = 90°$ is a bulk component. In Ref. 48, the MR proportional to $\sim B^2$ at $\theta = 90°$ was observed. In the data analysis, this component was subtracted from the MR obtained in other field angles. Since the samples used in Ref. 48 had a large carrier density, the large weight of the bulk conductance was reasonable with the $\sim B^2$ classical behavior of the MR supporting that analysis.

However, in our samples, as shown in Fig. 5, we did not find a valid argument to consider the MR at $\theta = 90°$ as the three-dimensional (3D) bulk contribution. The $\sim B^2$-type classical MR was absent at $\theta = 90°$. Instead, the MR behavior was reminiscent of the WAL effect. But, there is no consensus yet on whether the magnetoconductance (MC) correction (ΔG) of bulk carriers in TIs should follow the WAL or the weak localization (WL) behavior.[53,54] Thus, it is not clear whether the WAL-like $\Delta G(\theta = 90°)$ in our data is of bulk origin.

If the MR at $\theta = 90°$ corresponds to the 3D bulk contribution, in order to extract ΔG of the surface conducting channels, one has to use $\Delta G(\theta = 0°) - \Delta G(\theta = 90°)$ rather than $\Delta G(\theta = 0°)$ as used in the main text. But the bulk origin of $\Delta G(\theta = 90°)$ is not clear. On the other hand, the magnitude of ΔG at $\theta = 90°$ is sufficiently smaller than that at $\theta = 0°$ so that the discussion on the angle dependence of MR and the V_{bg} dependence of MR at $\theta = 0°$ in the main text is not affected even without subtracting $\Delta G(\theta = 90°)$. Therefore, we used the raw data for analysis of the gate dependence of WAL effects in Fig. 3 in main text.

It is not clear what caused this finite MR at $\theta = 90°$ in our TI flakes. It may have arisen from the sidewall surfaces of the thin crystal or even the in-plane MR of the surface conducting channels. There were some theoretical prediction of in-plane field-dependence MC correction for a 2D system, but not in the symplectic case.[64,65] Recently the in-plane field dependence of MC corrections in two dimensions is theoretically studied in the symplectic limit.[66] But it predicts in-plane MC corrections for a single TSS and cannot be applied directly to a system with multiple topological surface states which are coupled to bulk and topologically trivial surface states as in our devices.

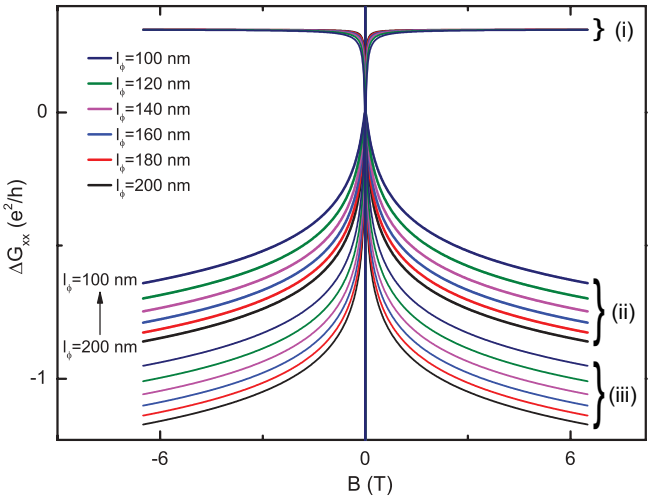

FIG. 6. (Color online) Sets of graphs of (i) the digamma function $-\frac{\alpha}{\pi}\psi(\frac{1}{2} + \frac{\hbar}{4el_\phi^2 B})$, (ii) the HLN function $\frac{\alpha}{\pi}[\ln(\frac{\hbar}{4el_\phi^2 B}) - \psi(\frac{1}{2} + \frac{\hbar}{4el_\phi^2 B})]$, and (iii) the logarithmic function $\frac{\alpha}{\pi}\ln(\frac{\hbar}{4el_\phi^2 B})$ of Eq. (D1) for $i = 1$, with $\alpha = 0.5$ and $l_\phi = 100$ nm $\sim$ 200 nm.

APPENDIX D: WEAK ANTILOCALIZATION ANALYSIS

Magnetoconductance (MC) correction of a 2D system in a symplectic limit can be expressed as Eq. (2) in the main text (HLN function). If there are two independent 2D conducting channels, the equation is expanded as follows:

$$\Delta G_{xx} = \sum_{i=1,2} \alpha_i \frac{e^2}{2\pi^2\hbar}\left[\ln\left(\frac{\hbar}{4el_{\phi,i}^2 B}\right) - \psi\left(\frac{1}{2} + \frac{\hbar}{4el_{\phi,i}^2 B}\right)\right], \tag{D1}$$

where ψ is the digamma function, e is the electron charge, α_i corresponds to the channel i with the phase relaxation length $l_{\phi,i}$.[32] If $l_{\phi,1} = l_{\phi,2} = l_\phi$, Eq. (D1) is simplified as follows:

$$\Delta G_{xx} = (\alpha_1 + \alpha_2)\frac{e^2}{2\pi^2\hbar}\left[\ln\left(\frac{\hbar}{4el_\phi^2 B}\right) - \psi\left(\frac{1}{2} + \frac{\hbar}{4el_\phi^2 B}\right)\right]. \tag{D2}$$

However, if $l_{\phi,1} \neq l_{\phi,2}$, the number of fitting parameters increases up to four with a larger standard error. We solved this problem by taking the following simple approximation.

In Fig. 6, the set of curves (i) represents the digamma function part, the set (iii) corresponds to the logarithmic function part, and the set (ii) corresponds to the sum of the two parts. Each function is plotted with $\alpha = 0.5$ and $l_\phi = 100 \sim 200$ nm. As displayed in Fig. 6, the digamma-function part is almost constant except in the weak-field region for different values of l_ϕ. Thus, the HLN expression is mostly determined by the logarithmic part. The digamma function causes a constant shift of the logarithmic function and removes the logarithmic divergence in zero field. Based on this fact, four parameters in Eq. (D1) can be reduced to two parameters as follows.

Let us define $l_{\phi,i}$ is the phase relaxation length of channel i ($i = 1,2$) with the corresponding coefficient α_i and l_ϕ^{eff} is the effective phase relaxation length with $\min\{l_{\phi,1}, l_{\phi,2}\} < l_\phi^{\text{eff}} < \max\{l_{\phi,1}, l_{\phi,2}\}$. Applying the approximated behavior of the

digamma function leads to

$$\begin{aligned}\Delta G_{xx} &= \alpha_1 \frac{e^2}{2\pi^2\hbar}\left[\ln\left(\frac{\hbar}{4el_{\phi,1}^2B}\right) - \psi\left(\frac{1}{2}+\frac{\hbar}{4el_{\phi,1}^2B}\right)\right] \\ &\quad + \alpha_2 \frac{e^2}{2\pi^2\hbar}\left[\ln\left(\frac{\hbar}{4el_{\phi,2}^2B}\right) - \psi\left(\frac{1}{2}+\frac{\hbar}{4el_{\phi,2}^2B}\right)\right] \\ &\approx \alpha_1 \frac{e^2}{2\pi^2\hbar}\left[\ln\left(\frac{\hbar}{4el_{\phi,1}^2B}\right) - \psi\left(\frac{1}{2}+\frac{\hbar}{4e\left(l_\phi^{\rm eff}\right)^2B}\right)\right] \\ &\quad + \alpha_2 \frac{e^2}{2\pi^2\hbar}\left[\ln\left(\frac{\hbar}{4el_{\phi,2}^2B}\right) - \psi\left(\frac{1}{2}+\frac{\hbar}{4e\left(l_\phi^{\rm eff}\right)^2B}\right)\right] \\ &= -(\alpha_1+\alpha_2)\frac{e^2}{2\pi^2\hbar}\psi\left(\frac{1}{2}+\frac{\hbar}{4e\left(l_\phi^{\rm eff}\right)^2B}\right) \\ &\quad + \frac{e^2}{2\pi^2\hbar}\left[\alpha_1\ln\left(\frac{\hbar}{4el_{\phi,1}^2B}\right) + \alpha_2\ln\left(\frac{\hbar}{4el_{\phi,2}^2B}\right)\right]. \end{aligned} \tag{D3}$$

The logarithmic part in Eq. (D3) becomes

$$\begin{aligned}&\alpha_1\ln\left(\frac{\hbar}{4el_{\phi,1}^2B}\right) + \alpha_2\ln\left(\frac{\hbar}{4el_{\phi,2}^2B}\right) \\ &= (\alpha_1+\alpha_2)\frac{\alpha_1}{(\alpha_1+\alpha_2)}\ln\left(\frac{\hbar}{4el_{\phi,1}^2B}\right) \\ &\quad + (\alpha_1+\alpha_2)\frac{\alpha_2}{(\alpha_1+\alpha_2)}\ln\left(\frac{\hbar}{4el_{\phi,2}^2B}\right) \\ &= (\alpha_1+\alpha_2)\left[\ln\left(\frac{\hbar}{4el_{\phi,1}^2B}\right)^{\frac{\alpha_1}{(\alpha_1+\alpha_2)}} + \ln\left(\frac{\hbar}{4el_{\phi,2}^2B}\right)^{\frac{\alpha_2}{(\alpha_1+\alpha_2)}}\right] \\ &= (\alpha_1+\alpha_2)\ln\left(\frac{\hbar}{4e\left(l_\phi^{\rm eff}\right)^2B}\right), \end{aligned} \tag{D4}$$

where $l_\phi^{\rm eff} \equiv l_{\phi,1}^{\frac{\alpha_1}{(\alpha_1+\alpha_2)}} l_{\phi,2}^{\frac{\alpha_2}{(\alpha_1+\alpha_2)}}$. Therefore, with Eq. (D3), the Eq. (D1) can be simplified as

$$\Delta G_{\rm xx} = \alpha\frac{e^2}{2\pi^2\hbar}\left[\ln\left(\frac{\hbar}{4e\left(l_\phi^{\rm eff}\right)^2B}\right) - \psi\left(\frac{1}{2}+\frac{\hbar}{4e\left(l_\phi^{\rm eff}\right)^2B}\right)\right] \tag{D5}$$

with $\alpha \equiv \alpha_1+\alpha_2$. Figure 7 shows the validity of this approximation.

In Fig. 7, the three curves (blue, black, and red online) correspond to the followings

$$\alpha_1[\ln(l_{\phi,1}) - \psi(l_{\phi,2})] + \alpha_2[\ln(l_{\phi,2}) - \psi(l_{\phi,2})] \tag{D6}$$

$$\alpha_1[\ln(l_{\phi,1}) - \psi(l_{\phi,1})] + \alpha_2[\ln(l_{\phi,2}) - \psi(l_{\phi,2})] \tag{D7}$$

$$\alpha_1[\ln(l_{\phi,1}) - \psi(l_{\phi,1})] + \alpha_2[\ln(l_{\phi,2}) - \psi(l_{\phi,1})], \tag{D8}$$

respectively. Here, $\psi(l_{\phi,i}) \equiv \psi(\frac{1}{2}+\frac{\hbar}{4el_{\phi,i}^2B})$ and $\ln(l_{\phi,i}) \equiv \ln(\frac{\hbar}{4el_{\phi,i}^2B})$. As displayed in Fig. 7, the deviation caused by different l_ϕ in digamma function can be recognized only in low fields. Furthermore, since $l_\phi^{\rm eff}$ has a value between $l_{\phi,1}$ and $l_{\phi,2}$, the deviation may be smaller than differences displayed in Fig. 7. Therefore, even with four parameters in different two channels, we can apply the one-channel HLN function with two parameters and the determined α and l_ϕ can be understood as $\alpha = \alpha_1+\alpha_2$ and $l_\phi = l_\phi^{\rm eff}$ as Eq. (D5).

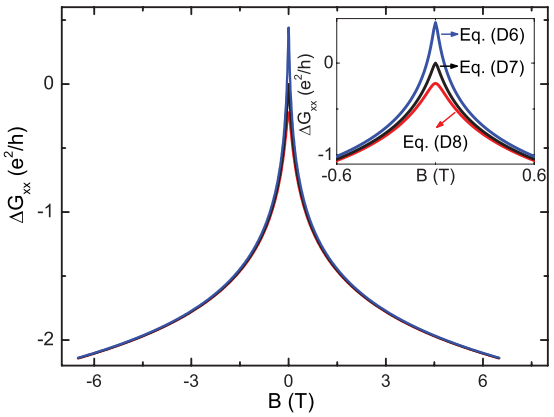

FIG. 7. (Color online) Three curves (blue, black, and red online) correspond to graphs of Eqs. (D6), (D7), and (D8) for $\alpha_1 = 1$, $\alpha_2 = 0.5$, $l_{\phi,1} = 100$ nm and $l_{\phi,2} = 200$ nm. Inset shows the expanded view in the low-field range.

APPENDIX E: $V_{\rm bg}$ INDEPENDENCE OF THE TOP-SURFACE CONDUCTANCE

Figure 8 shows the resistance variation of an 87-nm-thick BSTS flake (thickness of this flake is almost identical to that of the samples F3 and F4) as functions of back-gate ($V_{\rm bg}$) and top-gate (V_{tg}) voltages. This sample is not referred to in the main text. Except for the parallel shift in the resistance, the $V_{\rm tg}$ dependence of the resistance curves in Fig. 8 remains unaltered with varying $V_{\rm bg}$. Even the positions of the resistance spikes arising from the UCF effect do not change for different values of $V_{\rm bg}$. This feature indicates that the top-surface (bottom-surface) conductance is almost completely independent of $V_{\rm bg}$

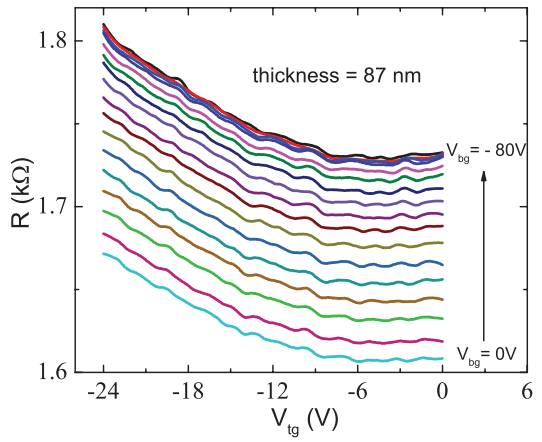

FIG. 8. (Color online) $V_{\rm bg}$ and V_{tg} dependencies of the resistance for the 87 nm-thick BSTS flake. Between two adjacent curves $V_{\rm bg}$ is varied by 5 V.

(V_{tg}). Since this flake and the samples F3 and F4 are of almost identical thickness we expect that the top-surface conductance of the two samples was independent of $V_{\rm bg}$, the fact of which is utilized in our analysis in the main text.

*hjlee@postech.ac.kr

[1] L. Fu and C. L. Kane, Phys. Rev. B **76**, 045302 (2007).
[2] L. Fu, C. L. Kane, and E. J. Mele, Phys. Rev. Lett. **98**, 106803 (2007).
[3] H. Zhang, C.-X. Liu, X.-L. Qi, X. Dai, Z. Fang, and S.-C. Zhang, Nature Phys. **5**, 438 (2009).
[4] M. Z. Hasan and C. L. Kane, Rev. Mod. Phys. **82**, 3045 (2010).
[5] X.-L. Qi and S.-C. Zhang, Rev. Mod. Phys. **83**, 1057 (2011).
[6] P. Roushan, J. Seo, C. V. Parker, Y. S. Hor, D. Hsieh, D. Qian, A. Richardella, M. Z. Hasan, R. J. Cava, and A. Yazdani, Nature (London) **460**, 1106 (2009).
[7] T. Zhang, P. Cheng, X. Chen, J.-F. Jia, X. Ma, K. He, L. Wang, H. Zhang, X. Dai, Z. Fang, X. Xie, and Q.-K. Xue, Phys. Rev. Lett. **103**, 266803 (2009).
[8] Z. Alpichshev, J. G. Analytis, J.-H. Chu, I. R. Fisher, Y. L. Chen, Z. X. Shen, A. Fang, and A. Kapitulnik, Phys. Rev. Lett. **104**, 016401 (2010).
[9] Y. Xia, D. Qian, D. Hsieh, L. Wray, A. Pal, H. Lin, A. Bansil, D. Grauer, Y. S. Hor, R. J. Cava, and M. Z. Hasan, Nature Phys. **5**, 398 (2009).
[10] Y. L. Chen, J. G. Analytis, J.-H. Chu, Z. K. Liu, S.-K. Mo, X. L. Qi, H. J. Zhang, D. H. Lu, X. Dai, Z. Fang, S. C. Zhang, I. R. Fisher, Z. Hussain, and Z.-X. Shen, Science **325**, 178 (2009).
[11] D. Hsieh, Y. Xia, D. Qian, L. Wray, J. H. Dil, F. Meier, J. Osterwalder, L. Patthey, J. G. Checkelsky, N. P. Ong, A. V. Fedorov, H. Lin, A. Bansil, D. Grauer, Y. S. Hor, R. J. Cava, and M. Z. Hasan, Nature (London) **460**, 1101 (2009).
[12] Z. Ren, A. A. Taskin, S. Sasaki, K. Segawa, and Y. Ando, Phys. Rev. B **84**, 165311 (2011).
[13] A. A. Taskin, Z. Ren, S. Sasaki, K. Segawa, and Y. Ando, Phys. Rev. Lett. **107**, 016801 (2011).
[14] T. Arakane, T. Sato, S. Souma, K. Kosaka, K. Nakayama, M. Komatsu, T. Takahashi, Z. Ren, K. Segawa, and Y. Ando, Nature Commun. **3**, 636 (2012).
[15] Z. Ren, A. A. Taskin, S. Sasaki, K. Segawa, and Y. Ando, Phys. Rev. B **85**, 155301 (2012).
[16] J. Chen, H. J. Qin, F. Yang, J. Liu, T. Guan, F. M. Qu, G. H. Zhang, J. R. Shi, X. C. Xie, C. L. Yang, K. H. Wu, Y. Q. Li, and L. Lu, Phys. Rev. Lett. **105**, 176602 (2010).
[17] J. G. Checkelsky, Y. S. Hor, R. J. Cava, and N. P. Ong, Phys. Rev. Lett. **106**, 196801 (2011).
[18] D. Kim, S. Cho, N. P. Butch, P. Syers, K. Kirshenbaum, S. Adam, J. Paglione, and M. S. Fuhrer, Nature Phys. **8**, 460 (2012).
[19] H. Steinberg, D. R. Gardner, Y. S. Lee, and P. Jarillo-Herrero, Nano Lett. **10**, 5032 (2010).
[20] D. Kong, Y. Chen, J. J. Cha, Q. Zhang, J. G. Analytis, K. Lai, Z. Liu, S. S. Hong, K. J. Koski, S.-K. Mo, Z. Hussain, I. R. Fisher, Z.-X. Shen, and Y. Cui, Nature Nanotechnol. **6**, 705 (2011).
[21] S. S. Hong, J. J. Cha, D. Kong, and Y. Cui, Nat. Commun. **3**, 757 (2012).
[22] Y. Wang, F. Xiu, L. Cheng, L. He, M. Lang, J. Tang, X. Kou, X. Yu, X. Jiang, Z. Chen, J. Zou, and K. L. Wang, Nano Lett. **12**, 1170 (2012).
[23] J. G. Analytis, J.-H. Chu, Y. Chen, F. Corredor, R. D. McDonald, Z. X. Shen, and I. R. Fisher, Phys. Rev. B **81**, 205407 (2010).
[24] K. Eto, Z. Ren, A. A. Taskin, K. Segawa, and Y. Ando, Phys. Rev. B **81**, 195309 (2010).
[25] J. G. Analytis, R. D. McDonald, S. C. Riggs, J.-H. Chu, G. S. Boebinger, and I. R. Fisher, Nat. Phys. **6**, 960 (2010).
[26] Z. Ren, A. A. Taskin, S. Sasaki, K. Segawa, and Y. Ando, Phys. Rev. B **82**, 241306 (2010).
[27] M. Petrushevsky, E. Lahoud, A. Ron, E. Maniv, I. Diamant, I. Neder, S. Wiedmann, V. K. Guduru, F. Chiappini, U. Zeitler, J. C. Maan, K. Chashka, A. Kanigel, and Y. Dagan, Phys. Rev. B **86**, 045131 (2012).
[28] J. Xiong, A. C. Petersen, D. Qu, Y. S. Hor, R. J. Cava, and N. P. Ong, Physica E **44**, 917 (2012).
[29] D.-X. Qu, Y. S. Hor, J. Xiong, R. J. Cava, and N. P. Ong, Science **329**, 821 (2010).
[30] Z. Ren, A. A. Taskin, S. Sasaki, K. Segawa, and Y. Ando, Phys. Rev. B **84**, 075316 (2011).
[31] J. G. Checkelsky, Y. S. Hor, M.-H. Liu, D.-X. Qu, R. J. Cava, and N. P. Ong, Phys. Rev. Lett. **103**, 246601 (2009).
[32] S. Hikami, A. I. Larkin, and Y. Nagaoka, Prog. Theor. Phys. **63**, 707 (1980).
[33] P. W. Anderson, Phys. Rev. **109**, 1492 (1958).
[34] G. Bergmann, Phys. Rep. **107**, 1 (1984).
[35] F. Xiu, L. He, Y. Wang, L. Cheng, L.-T. Chang, M. Lang, G. Huang, X. Kou, Y. Zhou, X. Jiang, Z. Chen, J. Zou, A. Shailos, and K. L. Wang, Nature Nanotechnol. **6**, 216 (2011).
[36] L. He, F. Xiu, X. Yu, M. Teague, W. Jiang, Y. Fan, X. Kou, M. Lang, Y. Wang, G. Huang, N.-C. Yeh, and K. L. Wang, Nano Lett. **12**, 1486 (2012).
[37] H. Cao, J. Tian, I. Miotkowski, T. Shen, J. Hu, S. Qiao, and Y. P. Chen, Phys. Rev. Lett. **108**, 216803 (2012).
[38] J. Xiong, Y. Luo, Y. Khoo, S. Jia, R. J. Cava, and N. P. Ong, Phys. Rev. B **86**, 045314 (2012).
[39] J. Chen, X. Y. He, K. H. Wu, Z. Q. Ji, L. Lu, J. R. Shi, J. H. Smet, and Y. Q. Li, Phys. Rev. B **83**, 241304 (2011).
[40] Y. S. Kim, M. Brahlek, N. Bansal, E. Edrey, G. A. Kapilevich, K. Iida, M. Tanimura, Y. Horibe, S.-W. Cheong, and S. Oh, Phys. Rev. B **84**, 073109 (2011).
[41] S. Matsuo, T. Koyama, K. Shimamura, T. Arakawa, Y. Nishihara, D. Chiba, K. Kobayashi, T. Ono, C.-Z. Chang, K. He, X.-C. Ma, and Q.-K. Xue, Phys. Rev. B **85**, 075440 (2012).
[42] H. Steinberg, J.-B. Laloë, V. Fatemi, J. S. Moodera, and P. Jarillo-Herrero, Phys. Rev. B **84**, 233101 (2011).
[43] G. Zhang, H. Qin, J. Chen, X. He, L. Lu, Y. Li, and K. Wu, Adv. Funct. Mater. **21**, 2351 (2011).
[44] J. J. Cha, D. Kong, S.-S. Hong, J. G. Analytis, K. Lai, and Y. Cui, Nano Lett. **12**, 1107 (2012).
[45] M. Bianchi, D. Guan, S. Bao, J. Mi, B. B. Iversen, P. D. C. King, and P. Hofmann, Nature Commun. **1**, 128 (2010).
[46] P. D. C. King, R. C. Hatch, M. Bianchi, R. Ovsyannikov, C. Lupulescu, G. Landolt, B. Slomski, J. H. Dil, D. Guan, J. L. Mi, E. D. L. Rienks, J. Fink, A. Lindblad, S. Svensson, S. Bao, G. Balakrishnan, B. B. Iversen, J. Osterwalder, W. Eberhardt,

F. Baumberger, and P. Hofmann, Phys. Rev. Lett. **107**, 096802 (2011).
[47]H. M. Benia, C. Lin, K. Kern, and C. R. Ast, Phys. Rev. Lett. **107**, 177602 (2011).
[48]H.-T. He, G. Wang, T. Zhang, I.-K. Sou, G. K. L. Wong, J.-N. Wang, H.-Z. Lu, S.-Q. Shen, and F.-C. Zhang, Phys. Rev. Lett. **106**, 166805 (2011).
[49]K. K. Choi, D. C. Tsui, and K. Alavi, Phys. Rev. B **36**, 7751 (1987).
[50]B. L. Altshuler, A. G. Aronov, and D. E. Khmelnitsky, J. Phys. C **15**, 7367 (1982).
[51]P. A. Lee and A. D. Stone, Phys. Rev. Lett. **55**, 1622 (1985).
[52]P. A. Lee, A. D. Stone, and H. Fukuyama, Phys. Rev. B **35**, 1039 (1987).
[53]I. Garate and L. Glazman, Phys. Rev. B **86**, 035422 (2012).
[54]H.-Z. Lu and S.-Q. Shen, Phys. Rev. B **84**, 125138 (2011).
[55]B. F. Gao, P. Gehring, M. Burghard, and K. Kern, Appl. Phys. Lett. **100**, 212402 (2012).
[56]P. Cheng, C. Song, T. Zhang, Y. Zhang, Y. Wang, J.-F. Jia, J. Wang, Y. Wang, B.-F. Zhu, X. Chen, X. Ma, K. He, L. Wang, X. Dai, Z. Fang, X. Xie, X.-L. Qi, C.-X. Liu, S.-C. Zhang, and Q.-K. Xue, Phys. Rev. Lett. **105**, 076801 (2010).
[57]T. Hanaguri, K. Igarashi, M. Kawamura, H. Takagi, and T. Sasagawa, Phys. Rev. B **82**, 081305 (2010).
[58]N. W. Ashcroft and N. D. Mermin, *Solid State Physics* (Thomson Learning, Ithaca, 1976).
[59]S. Kim, M. Ye, K. Kuroda, Y. Yamada, E. E. Krasovskii, E. V. Chulkov, K. Miyamoto, M. Nakatake, T. Okuda, Y. Ueda, K. Shimada, H. Namatame, M. Taniguchi, and A. Kimura, Phys. Rev. Lett. **107**, 056803 (2011).
[60]M. Lang, L. He, F. Xiu, X. Yu, J. Tang, Y. Wang, X. Kou, W. Jiang, A. V. Fedorov, and K. L. Wang, ACS Nano **6**, 295 (2012).
[61]C. Chen, S. He, H. Weng, W. Zhang, L. Zhao, H. Liu, X. Jia, D. Mou, S. Liu, J. He, Y. Peng, Y. Feng, Z. Xie, G. Liu, X. Dong, J. Zhang, X. Wang, Q. Peng, Z. Wang, S. Zhang, F. Yang, C. Chen, Z. Xu, X. Dai, Z. Fang, and X. J. Zhou, Proc. Natl. Acad. Sci. **109**, 3694 (2012).
[62]T. Ando, A. B. Fowler, and F. Stern, Rev. Mod. Phys. **54**, 437 (1982).
[63]A. B. Fowler, Phys. Rev. Lett. **34**, 15 (1975).
[64]S. Maekawa and H. Fukuyama, J. Phys. Soc. Jpn. **50**, 2516 (1981).
[65]B. L. Al'tshuler and A. G. Aronov, JETP Lett. **33**, 499 (1981).
[66]G. Tkachov and E. M. Hankiewicz, Phys. Rev. B **84**, 035444 (2011).